Downscaling satellite night-time light imagery while addressing the blooming effect

Nikolaos Tziokas, Ce Zhang, Alexandros Tziokas, Qunming Wang and Peter M. Atkinson

***Abstract*—In the past 20 years, improvements in night-time light (NTL) remote sensing have spurred a resurgence of interest in the mapping of human economic activity. Nevertheless, the full potential of NTL data for urban research is constrained by a relatively coarse spatial resolution and the blooming effect. Downscaling NTL data is a potential solution, aiming to obtain fine-resolution nocturnal data with high accuracy. Most existing remotely sensed image fusion techniques were developed for optical remote sensing images taken during the day. When NTL images are compared to optical images, they exhibit a greater quantity of dark (low value) pixels, higher levels of background noise, and a more obvious blooming effect. In this paper, we proposed a spatially non-stationary, geostatistical-based downscaling technique (random forest area-to-point Kriging) to downscale NTL data while accounting explicitly for the point spread function, thus, dealing with the blooming effect specific to NTL data. We compared several image fusion algorithms for downscaling while reducing the blooming effect. Numerical experiments on two megacities showed that downscaling was improved both numerically and visually by taking the PSF into consideration. During the RF regression, the R^2 increased and the RMSE decreased for both study regions, when accounting for the PSF. For the ATPK-based residual part, considering the PSF led to increased accuracy of prediction. The suggested methodology has the potential to increase the detail and accuracy of the NTL data available for modeling socioeconomic phenomena at the city scale, with wide potential for application in future socioeconomic research.**

***Index Terms*— Downscaling; Point spread function; Random forest; area-to-point Kriging; Satellite night-time light imagery; Urban remote sensing**

This paragraph of the first footnote will contain the date on which you submitted your paper for review, which is populated by IEEE. It is IEEE style to display support information, including sponsor and financial support acknowledgment, here and not in an acknowledgment section at the end of the article. For example, "This work was supported in part by the U.S. Department of Commerce under Grant 123456." *(Corresponding author: Ce Zhang, Peter M. Atkinson).*

Nikolaos Tziokas, Alexandros Tziokas and Peter M. Atkinson are with the Lancaster Environment Centre, Lancaster University, Bailrigg, Lancaster LA1 4YW, UK (e-mail: n.tziokas@lancaster.ac.uk, altziokas@gmail.com, pma@lancaster.ac.uk).

Ce Zhang is with the School of Geographical Sciences, University of Bristol, Bristol BS8 1SS, UK (e-mail: ce.zhang@bristol.ac.uk).

Qunming Wang is with the College of Surveying and Geo-Informatics, Tongji University, Shanghai 200092, China (e-mail: wangqm@tongji.edu).

Color versions of one or more of the figures in this article are available online at http://ieeexplore.ieee.org

I. INTRODUCTION

Anocturnal light (NTL) remote sensing data are acknowledged widely as being human-oriented, indicating the distribution and intensity of human activities. This contrasts with the more common optical remote sensing data, such as from Landsat and Sentinel, which focus primarily on the natural environment [1]. NTL remote sensing has gained significant interest due to its ability to bridge the gap between socioeconomic activity and the benefits of remote sensing data (standardization, repeat measurement, complete coverage). It is frequently utilized to derive objective and third-party socioeconomic indicators, such as on poverty [2], populations [3], urban built-up areas [4], GDP and energy consumption[5]. Urban areas, where economic activity tends to concentrate, are ideal places to study with the aim of addressing human-oriented issues such as sustainable development.

The Visible Infrared Imaging Radiometer Suite (VIIRS) Day/Night Band (DNB) is one of the most utilized sources of NTL data [6]. VIIRS offers fine temporal resolution (daily, monthly and yearly images), on-board calibration and the avoidance of saturated pixels, and it is free to acquire. In comparison, alternative NTL satellite products such as Luojia, Jinlin and DMSP-OLS, which have the advantages of either a finer spatial resolution or they extend further back in time, are commonly commercial products and expensive to purchase [7]. Notwithstanding the advantages of VIIRS, the utility of the data for scientific and practical applications is limited because of their ~500 m spatial resolution. Elvidge et al. [8] stated that a minimum spatial resolution of ~100 m should be used in urban related applications. This has led to issues (such as low accuracy and small correlation) when utilizing NTL imagery for mapping populations, built-up areas and economic indicators [6]. Moreover, night-time imaging has the overglow (or blooming) effect, equivalent to a large point spread function (PSF). Hence, there is a need for downscaling NTL imagery, and for mitigating the blooming effect.

Downscaling is the term used to describe a reduction in the pixel size of remotely sensed images in the context of remote sensing [9]. Downscaling has been undertaken using many methodologies and strategies, essentially aiming to increase the information richness of the downscaled images. Area-to-point Kriging (ATPK) is one such method [10]. It has the advantage of absolute coherence, which means that when the downscaled image is upscaled to the original coarse spatial resolution the results are identical. By including a (global)

regression term, Wang et al. [11] expanded ATPK and called it area-to-point regression Kriging (ATPRK). In ATPRK, covariates at a finer spatial resolution are employed in a (linear) regression model to predict the response variable. Then, the regression model's residuals are downscaled using ATPK. More recently, alternative regression methods have been used in the ATPRK model; nonetheless, the majority of the current algorithms for fusing remote sensing images are designed to fuse optical remote sensing images taken during the day. When NTL images are compared to optical remote sensing, they exhibit a greater quantity of dark pixels (low values) and more background noise [12], [13]. Consequently, it is of great interest to confirm the efficacy of conventional ATPK-based optical remote sensing techniques for VIIRS image downscaling.

Sufficiently large correlations between NTL and biophysical and/or socioeconomic covariates at a finer spatial resolution are required for multivariate downscaling. Population data, spectral indices and transport network data are examples. Regression models are fitted between the NTL data and aggregated (coarse resolution) covariates and then used with the fine-resolution covariates as inputs to predict NTL at the fine pixel size. According to Ye et al. [4] and Liu et al. [14], there is often a non-linear relationship between NTL and its covariates, which may render global models unsuitable. The capacity of machine learning (ML) algorithms to capture non-linear relations between NTL and fine-resolution covariates has been demonstrated recently [4], [12], [14], [15]. With several independent factors, deep neural network (DNN) and RF algorithms produced accurate predictions among the benchmarked techniques.

The point spread function (PSF) effect is widely seen in NTL remote sensing images [16]. It denotes that the signal for a certain pixel is the weighted sum of the contribution from its surrounding and internal pixels. This leads to a basic constraint on the information content of remote sensing images. Both the across-track and along-track directions are taken into consideration by the two-dimensional PSF function [17]. The instrument's optics, the detector, the electronics, atmospheric influences, and picture resampling are the primary causes of the PSF effect [18]. In places that are homogenous, the PSF effect might not be a major concern, but in diverse landscapes where mixed pixels predominate, it is essential. To the best of our knowledge, the PSF impact in NTL downscaling has not been studied yet. Therefore, searching for practical ways to lessen the PSF impact in NTL downscaling could provide guidance and potentially increase the accuracy for prediction.

In downscaling, the PSF of interest is not the measurement PSF, but rather the transfer function between images at the original coarse and target fine spatial resolutions [17]. The transfer function is different subtly to the measurement PSF. It is equivalent to the difference in convolution between the two PSFs used for measurement [17]. In the multi-variate scenario, additional data covering the same scene at the desired fine spatial resolution are available, despite the data being collected using several sensors or at different wavelengths. An important source of information for calculating the effective transformation PSF is the relationship between the coarse and fine resolution data. Research has established several approaches for PSF estimation [17]. However, the techniques were designed primarily for optical remote sensing. Solutions need to be identified that can both estimate the PSF for NTL data and work well in scenarios involving several fine covariates.

The major contributions of this paper include:

1. Random forest area-to-point Kriging (RFATPK) was demonstrated for downscaling NTL continua while reducing the PSF effect (multivariate case) and producing more accurate downscaling NTL predictions.
2. An existing solution was applied to estimate the effective transformation PSF for the multi-variate case of NTL downscaling. The solution estimates the PSF for the NTL band and is also suitable for dealing with multiple fine bands.
3. The proposed solution was applied in two case studies with different dominant land uses and different climate profiles to provide important guidance for their use in future applications.

The remainder of this paper is divided into four parts as follows. The concepts of RFATPK are introduced in Section 2, followed by the method of transformation PSF estimation. Section 3 presents the findings of the experiments conducted on two megacities. The results and associated problems are covered in Section 4, along with potential directions for future study. Section 5 draws conclusions of the paper.

II. STUDY AREA AND DATASETS

A. Study areas

Case study 1: Delhi, the capital of India, is situated along the Aravalli range, with Yamuna in the center and the Ganga River on its eastern border. Delhi has a semi-arid climate. It is a major international center and a highly populated metropolis on the Asian subcontinent, being home to over 16 million people (~10,400 people per km^2). Compared to the national average of 31.16%, 93% of the population lives in urban areas, indicating the city's fast industrialization and urbanization [19], [20].

Case study 2: As one of the largest metropolitan regions worldwide, the Los Angeles (LA) metropolitan area is the second largest in the USA. The U.S. Office of Management and Budget defines the Metropolitan Statistical Area (MSA) as the combination of Los Angeles and Orange counties, with a population of 9,819 million and a land area of 12,562 km^2 [21]. Because single-family detached homes are so common, the LA metropolitan region has a high degree of urbanization, a low population density, and fragmented retail centers that depend on intricate road networks [22]. Based on income, LA is classified by the World Bank as a high-income megacity [23]. The two study regions are shown in Figure 1. To demonstrate the methods more clearly in this paper we used subsets of the two megacities as the study regions.

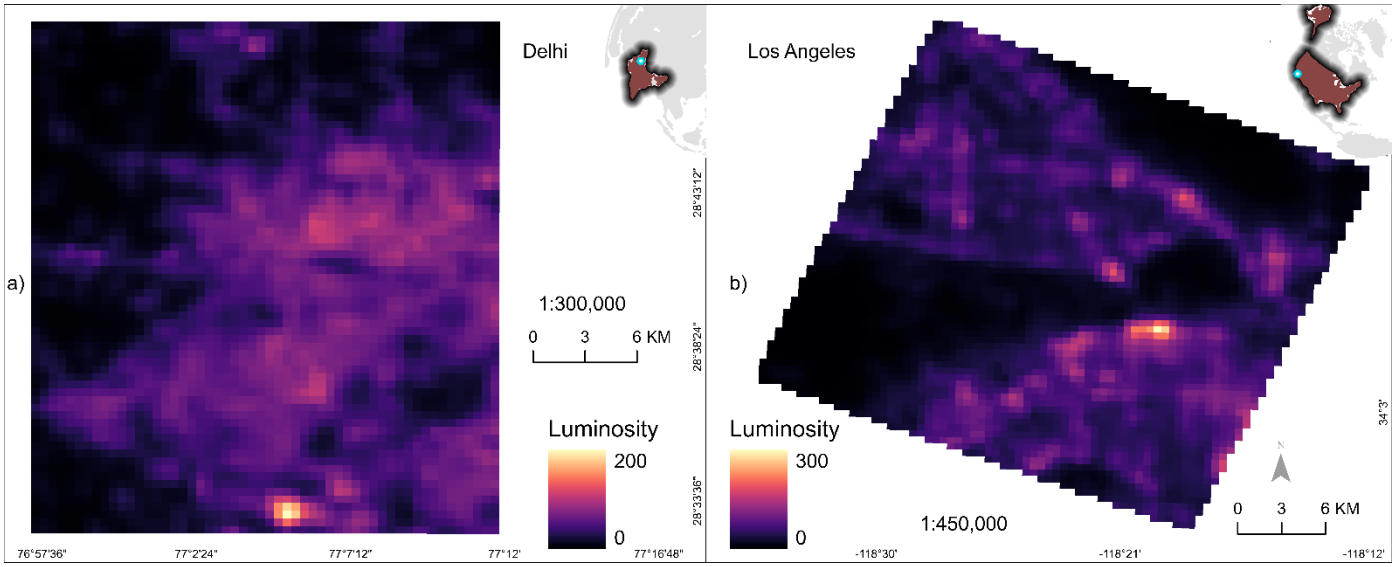

Figure 1. The VNP46A3 NTL image for a) Delhi and b) Los Angeles (LA). The darker colors indicate areas with no NTL luminosity while the brighter colors indicate areas with higher NTL luminosity.

B. Datasets

Multiple sources of data were used in this research.

1. Black Marbles monthly NTL composites (VNP46A3) were obtained from the NASA's website. The layer All_Angle_Composite_Snow_Free, which includes data collected during the snow-free time, was utilized in this paper. When compared to other composites (view zenith angle of 0°–20° and view zenith angle of 40°–60°), the all-angle composite has the most observations [24]. Monthly composite NTL products reduce the numbers of outliers and gaps caused by clouds, aerosols and poor data quality [25].
2. Mean monthly indices and spectral bands were used from Landsat 8. Appendix, Table 4 lists the spectral indices used in this research. Also, the total area of the rasterized building footprint dataset for the United States [26]. The data were downloaded using the Google Earth Engine (GEE) platform [27].
3. The Big Geospatial Data Platform OpenStreetMap (OSM) hosted on the Geofabrik website provided the road network for the research years ([28], accessed on June 10, 2023).
4. The Global Human Settlement Layers, which included the Global Human Settlement built-up surface grid (GHS-S), average building height (GHS-H) and population (GHS-P) were utilized only for Delhi ([30], accessed on June 10, 2023).
5. Annual population count statistics from the website of Oak Ridge National Laboratory ([31], accessed on 1 March 2023). We made the assumption that there were no annual changes to the population count. LandScan produces demographic statistics that are regarded as some of the best available.

III. METHODOLOGY

The proposed methodology is shown in Figure 2 as a sequence of actions intended to achieve the study goals. For downscaling without accounting for the PSF, the target variable and covariates were chosen first, and the covariates were upscaled to match the spatial resolution of the target variable (NTL). The residuals were then extracted as the difference between the RF regression model predictions and the observations. Third, ATPK was used to downscale the RF model residuals. Finally, the NTL raster layer with a spatial resolution of 130 m was created by combining the model prediction with the downscaled residuals.

To estimate the PSF (more specifically transfer function) of the NTL data the following steps were taken:

1. All fine spatial resolution covariates were convolved with a Gaussian PSF (with scale parameter σ_i) and spatially aggregated using a mean function to the coarse spatial resolution of the reference NTL.
2. For the NTL band, a RF regression model was fitted between the multiple aggregated covariates and the observed coarse image (e.g., the NTL). The R^2 was calculated.
3. Step 2 was conducted for all parameter candidates of σ (from 0.3 to 2 standard deviations * the pixel size, with step 0.1). For the visited coarse band, the optimal σ was estimated as the one leading to the largest R^2 in step 2.

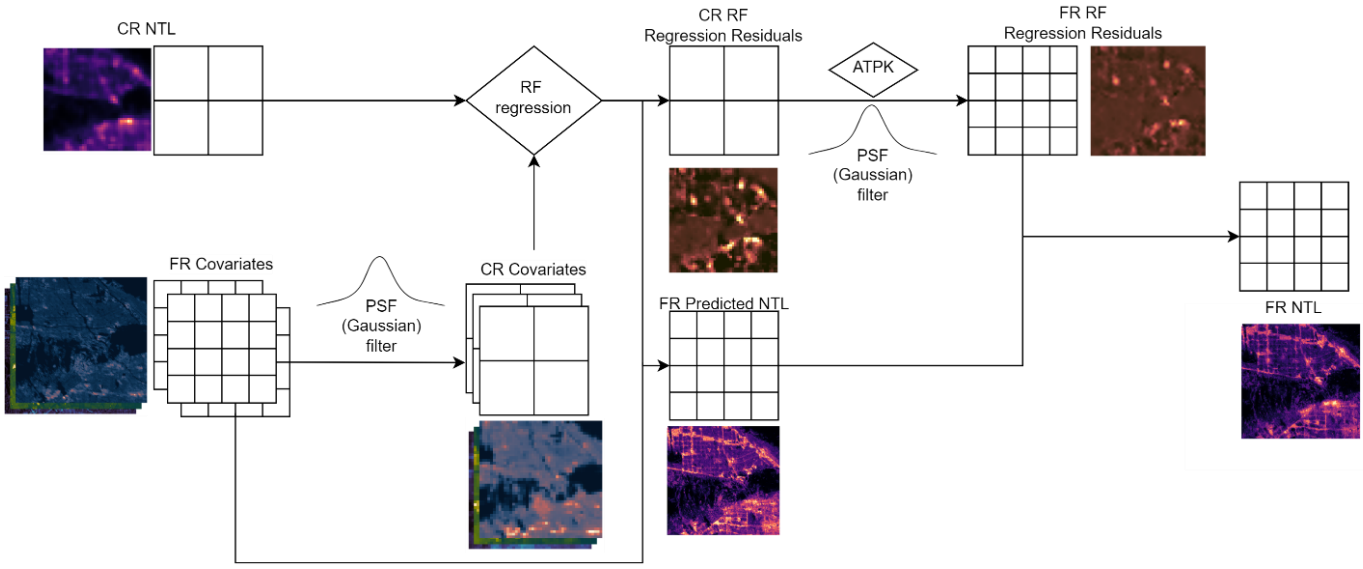

Figure 2. The methodology for applying RFATPK for downscaling NTL imagery. The acronyms CR and FR represent coarse resolution and fine resolution, respectively.

A. Preprocessing of spatial data

All data were re-projected to the EPSG:7760 and EPSG:3309 reference systems, for Delhi and LA, respectively. We removed tunnels from the provided road network vector data as we hypothesized that no light inside a tunnel can be detected from the sensor [37]. Then, we rasterized the data using a 130 m-by-130 m pixel size raster.

The Luojia1-01 imagery was, first, georeferenced using 30 carefully selected control points throughout each study region. The images were then re-projected to one of the projection systems, contingent upon the study region, and resampled using the spatial average to 130 m [38]. The following equation was then used to convert the image DN to radiance values, based on laboratory calibration data from the satellite data website:

$$r = \mathrm{DN}^{3/2} \cdot 10^{-10} \cdot w \quad (1)$$

where w is the bandwidth, measured in $\mathrm{Wm^{-2}sr^{-1}}$, DN is the digital number acquired by Luojia1-01, and r is the radiance value. Since Luojia1-01's radiometric range is 0.46-0.98 μm, w equals 0.52 μm.

The following data pre-processing procedures were applied to the monthly NTL product: (1) cloud removal and (2) outlier detection. In line with the cloud quality flag, we filtered the NTL radiance to retain only pixels with no cloud or cloud shadow detected. Moon illumination fractions were corrected, and anomalous pixels were examined using DNB quality flags once the clouds were cleared.

In this research, we used a variable selection approach to exclude covariates with low prediction power, even though RF can handle uncorrelated covariates with the response variable. This was accomplished using the R package *VSURF*. It involves a two-step process where the variables are first sorted based on a variable importance measure, and the less significant ones are removed. Second, a final subset is obtained by adding the sorted variables one after the other to the regression model. For further information, interested readers may consult Genuer et al. [39].

B. RFATPK

Because global regression models, such as the one used in ATPRK, makes the assumption that parameters are geographically invariant, it cannot fit relationships locally. Furthermore, it is possible that the global regression residual does not satisfy stationarity requirements (e.g., second-order stationarity), which would complicate the Kriging interpolation. The Random Forest (RF) is a non-parametric ensemble learning approach with high accuracy and resilience to multicollinearity, that was developed from the bagging algorithm [45]. Using a nonlinear regression model, the RFATPK approach considers both the geographical non-stationarity of the calculated residual NTL and the nonlinear correlation between NTL and the covariates. RFATPK formulation consists of a trend component as well as a regression residual component.

In the RFATPK technique, a regression model based on RF and independent variables at the coarse resolution is used initially to predict the geographic trend of NTL at the fine resolution. Next, a fine-scale prediction of the residual NTL is obtained by downscaling the coarse residual NTL using ATPK.

B1. RF to estimate the spatial trend

Due to its high accuracy and low risk of overfitting, RF has been used frequently in regression tasks [46]. A random vector generated separately and uniformly for every tree in the forest determines the values of each tree in a RF, which is a mixture of uncorrelated decision regression tree covariates. The RF regression approach was used in this research to increase the spatial resolution of NTL from 430 m to 130 m. Based on the nonlinear connection between the covariates calculated at 130 m spatial resolution from a variety of environmental and socioeconomic determinants, the original NTL data were downscaled. Following Wang et al.

[17] the 130 m spatial trend of NTL was predicted using the RF-based regression method which is summarized as follows: Initially, we applied a Gaussian filter to the covariates and then we spatially averaged them to match the NTL resolution. The filter's standard deviation ranged from 0.3 to 2 times the size of the coarse pixel, with a step of 0.1.

The RF regression approach, which can be stated using the following equation, was used to create the multivariate nonlinear regression model between the coarse NTL and the aggregated covariates:

$$\hat{Z}^{l}_{\text{Regression}}(x_0) = \text{RF}(\boldsymbol{ZK}_1, \boldsymbol{ZK}_2, \ldots, \boldsymbol{ZK}_l) + \boldsymbol{R} \quad (2)$$

The function RF(·) represents the multivariate nonlinear regression algorithm between NTL and the K covariates (showed in Table 1, depending on the megacity) constructed with the RF regression model and $\boldsymbol{R}$ are the coarse-resolution regression residuals. $\boldsymbol{ZK}_l$ is the coarse covariate produced by upscaling the corresponding fine resolution covariate (or spectral band) k using a PSF:

$$\boldsymbol{Z}k_l = \boldsymbol{Z}k_l * h_k \quad (3)$$

where h_k designates the transformation PSF between the fine and coarse resolution covariates. The RF algorithm was implemented using the R package, *ranger* [47].

Two-thirds of the covariates for each tree in the model were chosen as training samples using a bootstrap-based sampling technique to build the RF-based function approximation model. For each bootstrap-based sampling procedure, the remaining one-third of the inputs served as out-of-bag (OOB) data, meaning they were not used in the training process [48]. An important parameter is the number of regression trees (ntree) in the forest. As the number of trees increases, Oshiro et al. [49] claim that the model's performance eventually reaches a breaking point. Thus, the moment the OOB error reached its minimum, we stopped adding extra regression trees [46]. The RF-based nonlinear regression model in Eq. 2 can receive the 130 m independent variables as direct input. Next, it is possible to compute the NTL's downscaled spatial trend at a resolution of 130 m.

B2. ATPK for downscaling residuals

In the next step of RFATPK, the coarse-resolution residuals $\boldsymbol{R}$ yielded in the regression model in the initial step are sharpened to a fine resolution using the ATPK algorithm:

$$\hat{Z}^{l}_{Residuals}(x_0) = \sum_{i=1}^{N} \lambda_i \boldsymbol{R}(x_i), \quad \text{s.t.} \quad \sum_{i=1}^{N} \lambda_i = 1 \quad (4)$$

where $\boldsymbol{R}(x_i)$is the residual for the ith neighbor. The weights are calculated according to the Kriging matrix:

$$\begin{bmatrix} \boldsymbol{\gamma}_{\text{CC}} & \mathbf{1}^T \\ \mathbf{1} & 0 \end{bmatrix} \begin{bmatrix} \boldsymbol{\lambda} \\ \theta \end{bmatrix} = \begin{bmatrix} \boldsymbol{\gamma}_{\text{FC}} \\ 1 \end{bmatrix} \quad (5)$$

where $\boldsymbol{\gamma}_{\text{CC}} = [\gamma_{\text{CC}}(\mathbf{s}_{ij}),\ i = 1, \ldots, N,\ j = 1, \ldots, N]$ is an $N \times N$ matrix of coarse-to-coarse semivariances between the coarse resolution pixels centered at $\mathbf{x}_i$ and $\mathbf{x}_j$ ($\mathbf{s}$ is the Euclidean distance between the centroids of any random two pixels), $\boldsymbol{\gamma}_{\text{FC}} = [\gamma_{\text{FC}}(\mathbf{s}_{0i}),\ i = 1, \ldots, N]^T$ is an $N \times 1$ vector of fine-to-coarse semivariances between the fine and coarse resolution pixels centered at $\mathbf{x}_0$ and $\mathbf{x}_i$, $\boldsymbol{\lambda} = [\lambda_i,\ i = 1, \ldots, N]^T$ is an $N \times 1$ vector of weights for the N coarse resolution neighbors, $\mathbf{1}$ is a $1 \times N$ vector of ones, and θ denotes the Lagrange multiplier (Wang et al., 2020).

Assume that h_k is the PSF utilized for transforming the fine-resolution covariates to the coarse spatial resolution. The semivariograms $\gamma_{\text{FC}}(\mathbf{s})$ and $\gamma_{\text{CC}}(\mathbf{s})$ used in Eq. 5 are computed by convolving the fine-to-fine semivariogram (represented as $\gamma_{\text{FF}}(\mathbf{s})$) between any two fine resolution pixels. The $\gamma_{\text{FF}}(\mathbf{s})$, $\gamma_{\text{FC}}(s)$ and $\gamma_{\text{CC}}(\mathbf{s})$ semivariograms are a function of the distance and direction vector $\mathbf{s}$ (which is called lag in the field of geostatistics), that is, they are influenced specifically by separation distance and direction and not by the specific locations of the pixels. Also, the semivariogram can be seen as a 2-D image centered at (0, 0), which is built from values in all directions and at multiple distances. In this sense, $\gamma_{\text{FC}}(\mathbf{s})$ and $\gamma_{\text{CC}}(\mathbf{s})$ are computed as:

$$\gamma_{\text{FC}}(\mathbf{s}) = \gamma_{\text{FF}}(\boldsymbol{s}) * h_C(\mathbf{s}) = \int_{x \in V(\mathbf{s})} \gamma_{\text{FF}}(\mathbf{x}) \cdot h_C(\mathbf{s} - \mathbf{x}) d\mathbf{x} = \sum_{x_1 = s_1 - w_1}^{s_1 + w_1} \sum_{x_2 = s_2 - w_2}^{s_2 + w_2} \gamma_{\text{FF}}(x_1, x_2) \cdot h_C(s_1 - x_1, s_2 - x_2) \quad (6)$$

$$\gamma_{\text{CC}}(\mathbf{s}) = \gamma_{\text{FF}}(\mathbf{s}) * h_C(s) * h_C(-\mathbf{s}) = \gamma_{\text{FC}}(\mathbf{s}) * h_C(-\mathbf{s}) = \int_{\mathbf{x} \in V(\mathbf{s})} \gamma_{\text{FC}}(\mathbf{x}) \cdot h_C(\mathbf{x} - \mathbf{s}) d\mathbf{x} = \sum_{x_1 = s_1 - w_1}^{s_1 + w_1} \sum_{x_2 = s_2 - w_2}^{s_2 + w_2} \gamma_{\text{FC}}(x_1, x_2) \cdot h_C(x_1 - s_1, x_2 - s_2) \quad (7)$$

where * indicates the convolution operator, $V(\mathbf{s})$ is the spatial coverage (with an extent of $2w_1 + 1$ by $2w_2 + 1$ fine resolution pixels) of the PSF centered at point $\mathbf{s} = (s_1, s_2)$, and $\mathbf{x} = (x_1, x_2)$ is the center of the fine resolution pixel within coverage $V(\mathbf{s})$ in the 2-D semivariogram image: $\gamma_{FF}(\mathbf{s})$ or $\gamma_{FC}(\mathbf{s})$.

The fine-to-fine semivariogram $\gamma_{FF}(\mathbf{s})$ is unknown and it can be approximated by deconvolution of the areal semivariogram calculated from the original coarse spatial resolution image [42]–[44]. The prime solution is determined as the one that, once convolved according to Eq. 7, is the same as the known areal semivariogram. It should be noted that here the corresponding semivariograms are of the residuals as in ATPRK, not of the original variable as in ATPK. Readers interested in a more in-depth discussion of the deconvolution methodology utilized in this research can be found in Wang et al. [11].

The benefit of ATPK, namely the perfect coherence property, which was illustrated theoretically by Wang et al. (2015), is carried over to RFATPK:

$$\hat{\mathbf{Z}}^{l}_{F} * h_C = \mathbf{Z}^{l}_{C} \quad (8)$$

The PSF effect is considered in both regression modeling (see Eq. 3) and ATPK-based residual downscaling. With respect to the former, different PSFs will result in different upscaled images $\boldsymbol{Z}^{k}_{C}$ and different regression models (i.e., different predictions from $\hat{\mathbf{Z}}^{l}_{\text{Regression}}$). This means that, different residuals, $\mathbf{R}^{l}_{C}$, will be produced from the regression model conditional upon the choice of PSF. This will have a direct effect on the prediction of $\hat{Z}^{l}_{\text{Residuals}}(\mathbf{x})$ in ATPK-based residual downscaling.

It is clear from the previously discussed downscaling approach utilizing RFATPK that the transformation PSF

relating images at different resolutions to each other, rather than the PSF of the original measurements, plays a crucial role in modeling semivariograms at different spatial scales and should not be disregarded. It is crucial to ascertain the transformation PSF for downscaling in advance because it may not be known in real-world situations. Finding methods that approximate the appropriate transformation PSF for the multivariate scenario, while taking into account the availability of auxiliary data at the requisite fine spatial resolution, is a more feasible strategy.

B3. PSF estimation

It is known that there always exists a statistical relation among different spectral bands covering the same region, and largely for spectral bands with similar wavelengths. It is hypothesized that the single coarse resolution image $\boldsymbol{Z}K_l$ can be defined as a linear combination of the set of bands $\boldsymbol{Z}K_l(k = 1, ..., K)$ created by upscaling the existing fine spatial resolution images $\boldsymbol{Z}k_l$ $(k = 1, ..., K)$ at other wavelengths:

$$\boldsymbol{Z}K_l = \sum_k a_k \left(\boldsymbol{Z}k_l * h_k\right) + \boldsymbol{\varepsilon} \tag{9}$$

As such, the best scale transformation PSF h_k for image (or spectral band) $\boldsymbol{Z}K$ can be determined as the one reducing the fitting error $\boldsymbol{\varepsilon}$:

$$\hat{h}_c^l = \underset{h_c^l}{arginf} f\left(\mathbf{z}_c^l - \sum_k a_k(\boldsymbol{Z}k_l * h_k)\right) \tag{10}$$

where f is an operator for determining the fitting error and it is computed by the fitting regression model (e.g., the classical global linear regression model, RF regression, etc.). Each coarse band is assigned a distinctive optimal PSF h_k, which varies for the several coarse resolution bands.

C. Urban socioeconomic applications

A major application of NTL imagery is its use as a proxy measure with which to study socioeconomic disparities. Here, we use the sharpened NTL imagery as a proxy for such phenomena to illustrate the benefits of our proposed approach to downscaling NTL data.

Previous research has already highlighted the superiority of the downscaled NTL compared to coarse scale counterparts, to some extent [12]. In this study, to further highlight the benefits of the geostatistical model, RFATPRK, we conducted experiments using two socioeconomic variables. These were (1) the Human Development Index (HDI) and (2) income, measured in $1,000. More specifically, a linear regression model was fitted using the socioeconomic variables and the (downscaled with and without a PSF) NTL data, and their coefficients of determination (R^2) were compared.

Yearly data for the two indices for both megacities were acquired from the Global Data Lab website ([50], accessed September 10, 2023). Then, using the LC data and the built-up class as a mask, we removed the non-built-up areas from the NTL images. The reason for doing so is that the exclusion of non-residential areas can increase the accuracy of predicting of socioeconomic variables [51].

IV. RESULTS

A. Significance of the selected variables for the RF regression

Table 1 shows the variable importance derived from RF in two megacities. It is important to note that while this importance score provides a relative evaluation of the contributions of the input variables, it is not the same as the correlation coefficient. Different covariates were used for the two megacities, with some similarities.

Table I

RF regression variable importance scores across all megacities.

LA	AGBH	BRBA	DBI	GHS	HFP	MNDWI	NBI	NDVI	POP	TA
	0.16	0.17	0.22	0.21	0.44	0.9	0.08	0.15	0.15	0.14
Delhi	AGBH	BAEI	BRBA	GHC	GHS	GNDVI	HFP	MNDWI	NDVI	POP
	0.80	0.16	0.48	0.51	0.43	0.47	0.77	0.44	0.46	0.98

The contributions of the built-up spectral indices are shown to be greater than those of any other variable in both areas, except for MNDWI. This implies that the built-up areas can represent the NTL intensity reasonably well. In addition, the socioeconomic covariate (POP), shows a significant inconsistency between the two megacities, and the same is true for AGBH.

For the megacity of LA, the spatial distribution of NTL is highly controlled by the MNDWI and built-up indices, such as the DBI. For the megacity of Delhi, the POP is the dominant covariate, and again, the built-up indices showed a significant importance. The vegetation-based spectral indices also illustrated greater significance for this megacity compared to LA. For both cases, the built environment, which is perceived as an indicator of buildings and road networks in cities, on average, had the higher importance.

Several inter-correlated variables may serve as surrogates, and since these importance scores fluctuate with the number of input variables - that is, when input variables are added or removed - they may provide support for the choice of input variables with a larger correlation.

B. Validation of the PSF approximation

The proposed technique was used to fuse monthly NTL monthly composites from 2015 to 2020. The goal of this experiment was to fuse the fine resolution 130 m covariates with the monthly NTL images to downscale NTL to 130 m. For the NTL, the Gaussian PSF was used.

LA and Delhi served as the research locations for validating the suggested geostatistical filter-based image enhancement technique. With this design, that is, two megacities located in different geographic regions with different climates, as well as different numbers of images used for creation of the monthly composite, it is possible to explore the different effects that these parameters (i.e., climate and number of images) have on the capability of the proposed

method. The minimum number of clear pixels per monthly composite pixel was at least seven.

The RF regression model was evaluated quantitatively using the R^2, and the RFATPK-based downscaling strategy was evaluated using the root-mean-squared error (RMSE).

C. RF regression

Based on Wang et al. [17], the Gaussian filter's ideal σ (standard deviation) is the one that produces the largest R^2 in the (RF) regression. The results for the cities of Delhi and LA in 2018 as an example year are listed below.

Figure 3 illustrates the R^2 of the RF model plotted against PSF size (i.e., σ) for the megacities of Delhi (plot a) and LA (plot b), respectively. RF could explain more than 96% of the variation in NTL intensity for Delhi and more than 85% for LA.

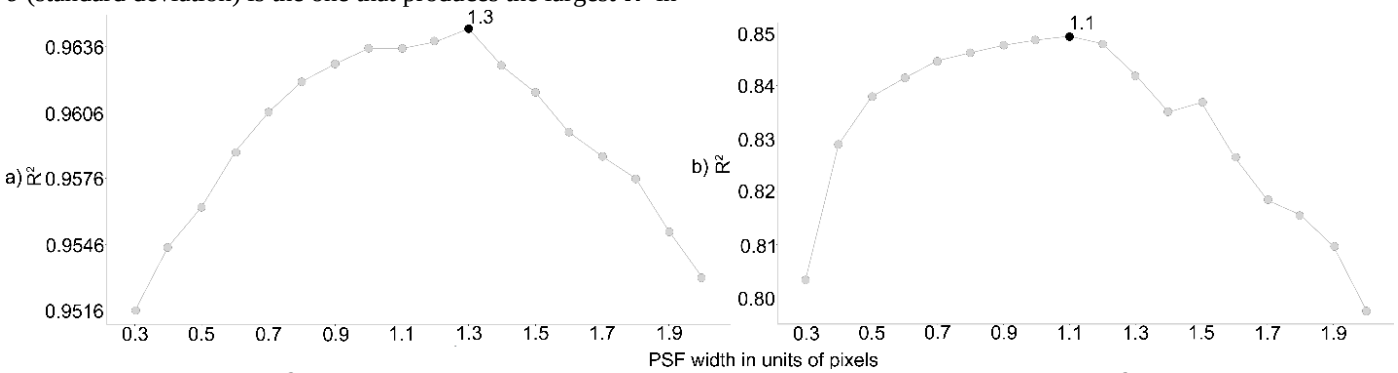

Figure 3. Plot of the RF R^2 (y-axis) against PSF width (x-axis). The PSF width that yielded the largest R^2 is plotted in black. a) R^2 for Delhi, b) R^2 for LA.

The optimal parameter maximizing the R^2 was selected from the pool composed of 17 values (0.3, 0.4, …, and 2 coarse pixels). For LA, the largest R^2 value in the RF regression model was σ = 1.1 while for Delhi it was σ = 1.3. The results indicate that after a certain value (1.1 and 1.3 coarse pixels) the larger the width of the PSF the smaller the R^2. The results are comparable to the work of Wang et al. [17] where they downscaled day-time satellite sensor imagery and found similar behavior.

D. RFATPK results

Luojia NTL data were used to assess the PSF parameter estimation. The assessment was carried out using a two-step process. The preservation of spatial patterns in the downscaled NTL, the validation data (i.e., Luojia's NTL), and the original coarse resolution NTL data were first visually inspected and compared. After that, the downscaled NTL data were subjected to a Gaussian filter (with σ varying from 0.4 to 2), and the RMSE was computed using the validation data. This was done because, despite the validation data being regarded as "true" data (i.e., perfect data without errors) the measurement PSF effect also has a significant impact on Luojia's images [52]. Figures 4 and 5 for Delhi and LA, respectively, demonstrate this, where it can be seen that the downscaled NTL images are clearly sharper than the Luojia reference images.

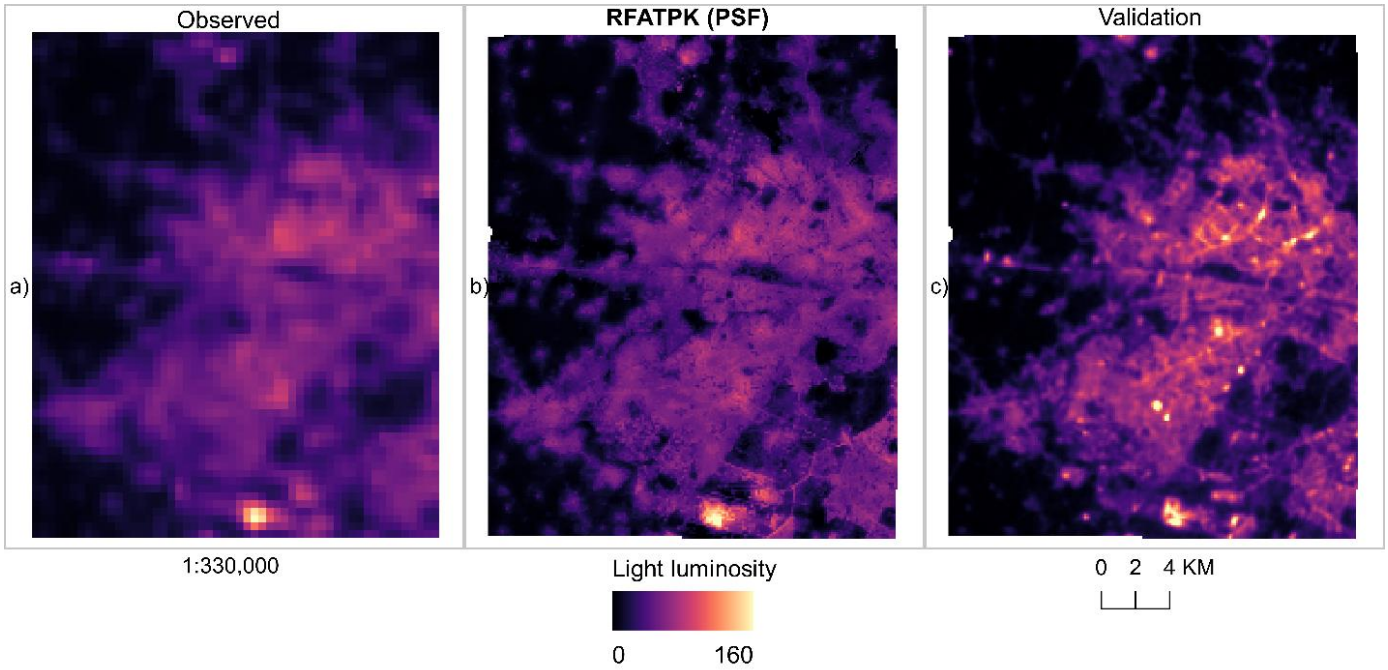

Figure 4. Downscaling results of the NTL imagery (Delhi) using the selected PSF width (1.3 coarse pixel size). a) is the reference NTL image at the coarse spatial scale, b) is the downscaled NTL image, c) is the validation image, Luojia.

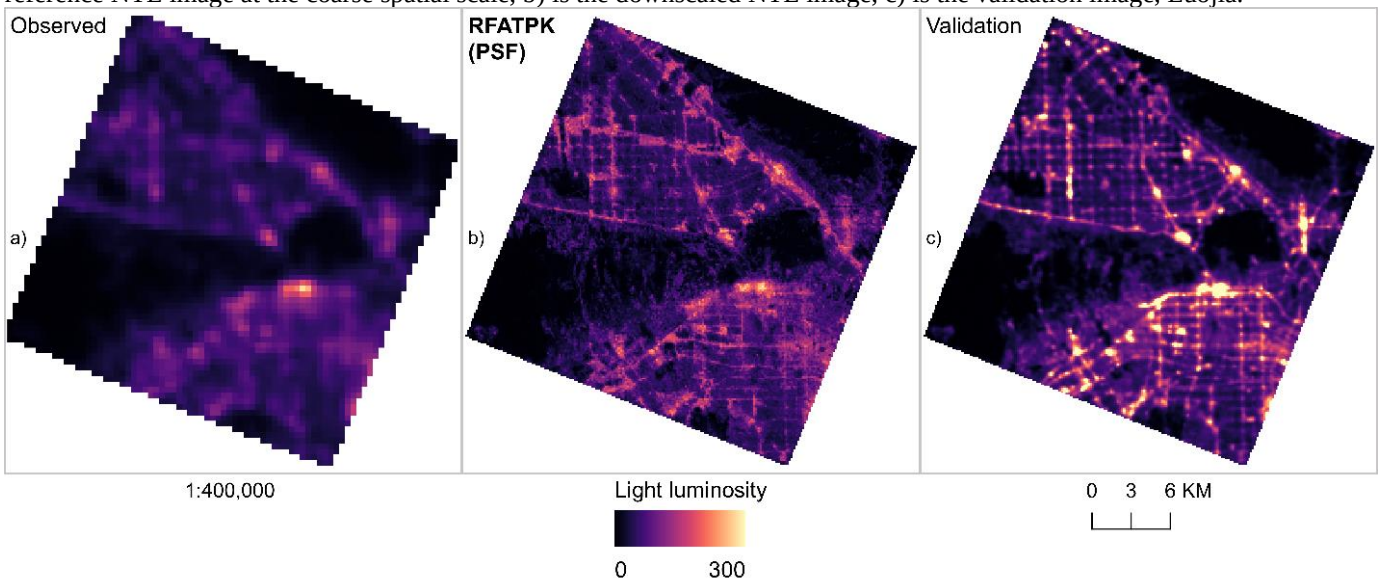

Figure 5. Downscaling results of the NTL imagery (LA) using the selected PSF width (1.1 coarse pixel size). a) is the reference NTL image at the coarse spatial scale, b) is the downscaled NTL image, c) is the validation image, Luojia.

From Figures 4b and 5b, the downscaling results can be compared to the reference NTL (a) and the validation NTL (c). In both megacities the predicted NTL captures the spatial variability of brightness reasonably well, and visually the results are more comparable to the validation NTL. Moreover, the spatial structure of the study sites (e.g., road network) is well defined in the downscaled images and is even more obvious in the maps (b), compared to the validation data.

A highlight are the areas with high light intensity. For both megacities these areas represent the airport: for Delhi this is located in the south part of the image (Figs. 4 and 6, (a)), while for LA the airport is in the west of the image (Figs. 5 and 7, (a)). The other bright spots in LA are dense road networks. In the downscaled images (maps (b) in Figs. 5 and 7) the bright spots were maintained, but their difference in brightness compared to other land uses is not as obvious as in the Luojia images. The results indicate that over complex terrains (i.e., different land uses) RF struggles to model the differences in brightness. The results are in line with other research downscaling land surface temperature data where similar behavior was observed [53].

Figures 6 and 7 illustrate the differences between the downscaled NTL images without accounting for the PSF and with the PSF for Delhi (Fig. 6) and LA (Fig. 7), respectively.

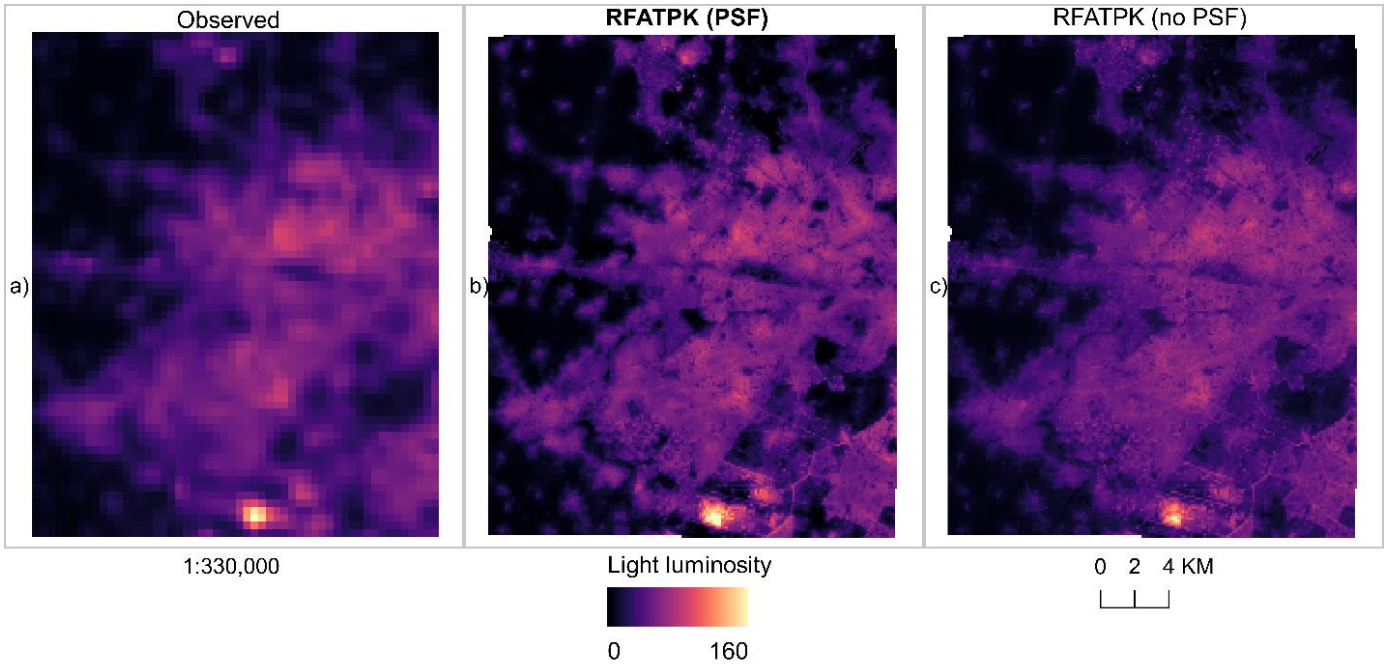

Figure 6. Downscaling results for the 130 m NTL image for Delhi. (a) 430 m coarse image. (b) RFATPK with PSF. (c) RFATPK without PSF.

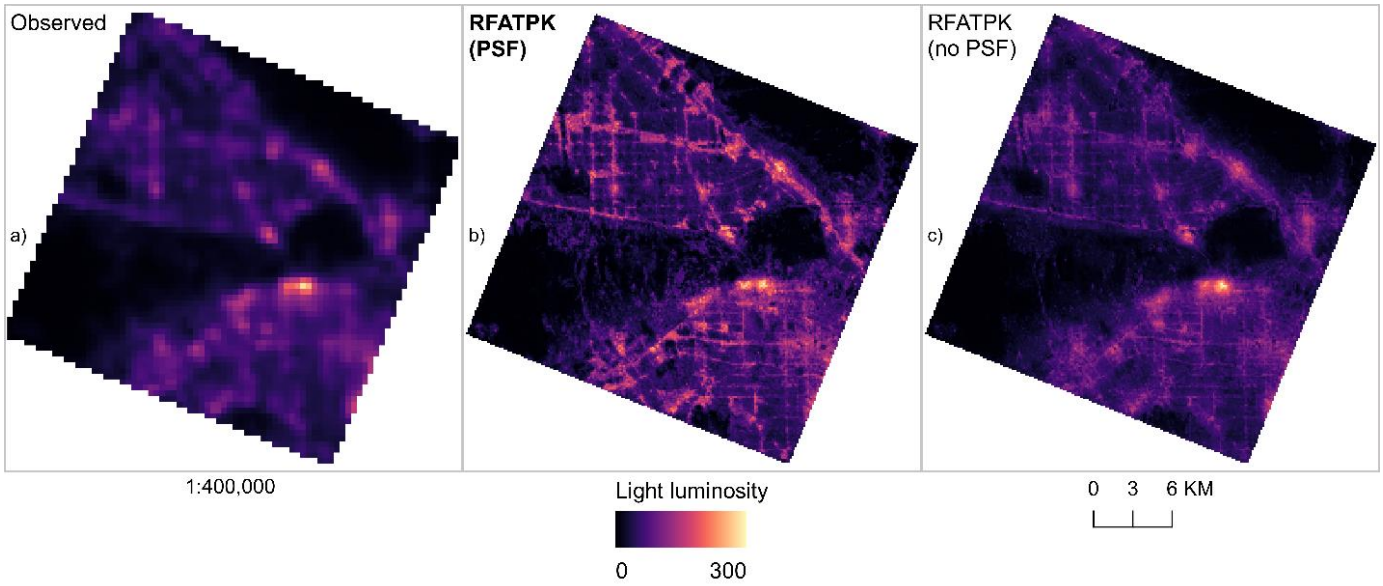

Figure 7. Downscaling results for the 130 m NTL image for LA. (a) 430 m coarse image. (b) RFATPK with PSF. (c) RFATPK without PSF.

Predictions made with the PSF considered are visually much clearer than those made without it, and shows more spatial information (such as the road network). Additionally, there is a greater contrast between parts that are lit and those that are not, indicating that the blooming effect has been lessened by taking the PSF into account.

Moreover, we provided the results without ATPK-based residual downscaling to further validate the effectiveness of RFATPK. The validation was done using Luojia images as reference.

Table II
Comparison of the RFATPK and RF (without ATPK-based residual downscaling) methods using a Luojia image as reference.

Megacity	**Method**	**Metric**	
		R^2	RMSE
Delhi	RFATPK	0.82	16.11
	RF	0.80	16.93
LA	RFATPK	0.72	48.64
	RF	0.68	51.67

Based on Table 2, it can be seen that for both megaregions, the predictions are more accurate when considering the ATPK-based residual downscaling in terms of R^2 and RMSE. More

specifically, the R^2 for Delhi and LA was 0.82 and 0.72 for the RFATPK method, respectively. In comparison, the same metric was 0.80 and 0.62 for the RF method. For the city of LA, the difference between the R^2 was 0.4, with the RFATPK producing more accurate predictions. The same behaviour was observed for the RMSE, with the RMSE being lower for the RFATPK method for both areas.

E. Quantitative validation

For quantitative validation the downscaled images were filtered using a Gaussian PSF (i.e., upscaling filter) to simulate the measurement PSF of the Luojia images and, thus, take the prediction result closer to the Luojia reference. The size of the filter's standard deviation ranged from 0.4 to 2 times the pixel size (130 m) for LA and Delhi. Then the filtered images were compared to Luojia's NTL and the RMSE (in units of reflectance) was computed. The results are shown in plot 8 below, for Delhi and LA, respectively.

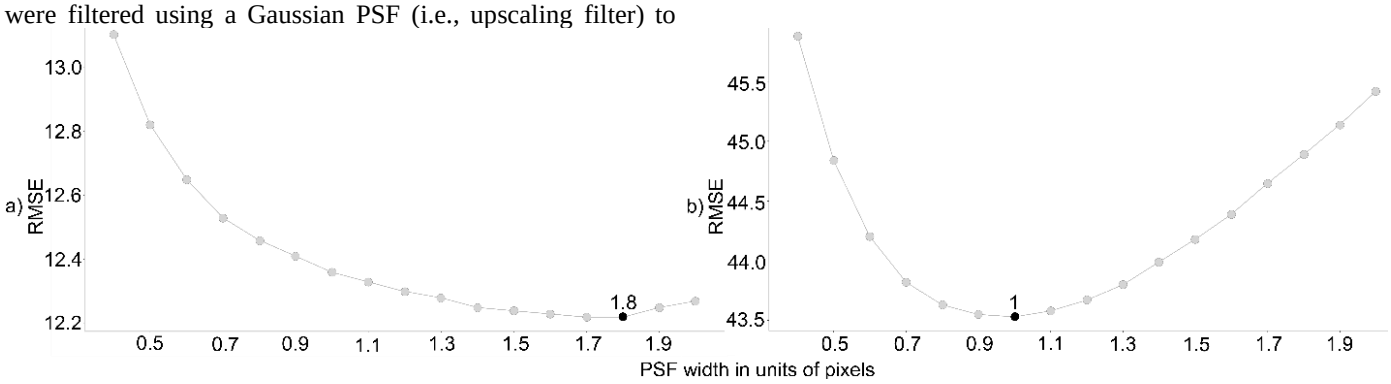

Figure 8. Plot of RMSE (predicted NTL and Luojia) against PSF width used for validation of the downscaled NTL image. The black symbol indicates the PSF width that yielded the smallest RMSE value.

In both cases, as the PSF width increases, the RMSE decreases, up to the point of 1.8 for Delhi and 1 for LA. After that, the RMSE starts to rise. The optimal PSFs differ from those identified in Figure 3 because they measure different PSFs. The optimal PSFs identified here relate to the upscaling needed to match to the Luojia images which themselves are contaminated with their own blooming effect. This is different to the PSF needed to downscale the NTL images.

For quantitative comparison of the downscaled NTL with the transformation PSF (denoted as $RFTPK_U$), we used the filtered downscaled predictions (i.e., the ones presented in Figure 8) and the predictions without accounting for the PSF (denoted as $RFATPK_D$). Moreover, we downscaled the NTL using $ATPRK_D$ and an allocation of pixel values of the coarse resolution NTL to a grid of 130m (called Allocation-based downscaling). Luojia's NTL is used as the validation dataset and the results are presented in Table 3.

Table III

Quantitative comparison (in terms of R^2 and RMSE) of the downscaling results for the NTL images for the two megacities. In bold are the results with the largest R^2 and smallest RMSE.

Megacity	**Method**	**Index**	
		R^2	RMSE
Delhi	$RFATPK_D$	0.8097	12.2568
	$RFATPK_U$	**0.8109**	**12.2158**
	$ATPRK_D$	0.8023	12.4906
	Allocation	0.8018	12.5075
Los Angeles	$RFATPK_D$	0.6051	44.1739
	$RFATPK_U$	**0.6164**	**43.5349**
	$ATPRK_D$	0.5970	44.6254
	Allocation	0.6000	44.4544

Based on Table 2, for the megacity of Delhi, it can be observed that the highest R^2 and lowest RMSE was achieved when using the proposed approach ($RFATPK_U$). 0.8109 and 12.2158 were the values for R^2 RMSE, respectively. For LA, again, $RFATPK_U$ achieved the best results, with 0.6164 and 43.5349 for the R^2 and RMSE. Apart from the quantitative comparison a visual one was considered. Moreover, the Allocation-based downscaling performed better than ATPRK in LA, but RFATPK (with and without the PSF) outperformed the other methods in both megaregions. This is because the study sites there are multiple land cover/uses (e.g., airports, water bodies, vegetation), thus, a global regression model, such as the linear regression model in $ATPRK_D$, cannot capture the local spatial variability adequately. RF on the other hand, as a local model, can model the variations.

The maps below depict a visual comparison of the downscaling approaches for Delhi (Figure 9) and LA (Figure 10).

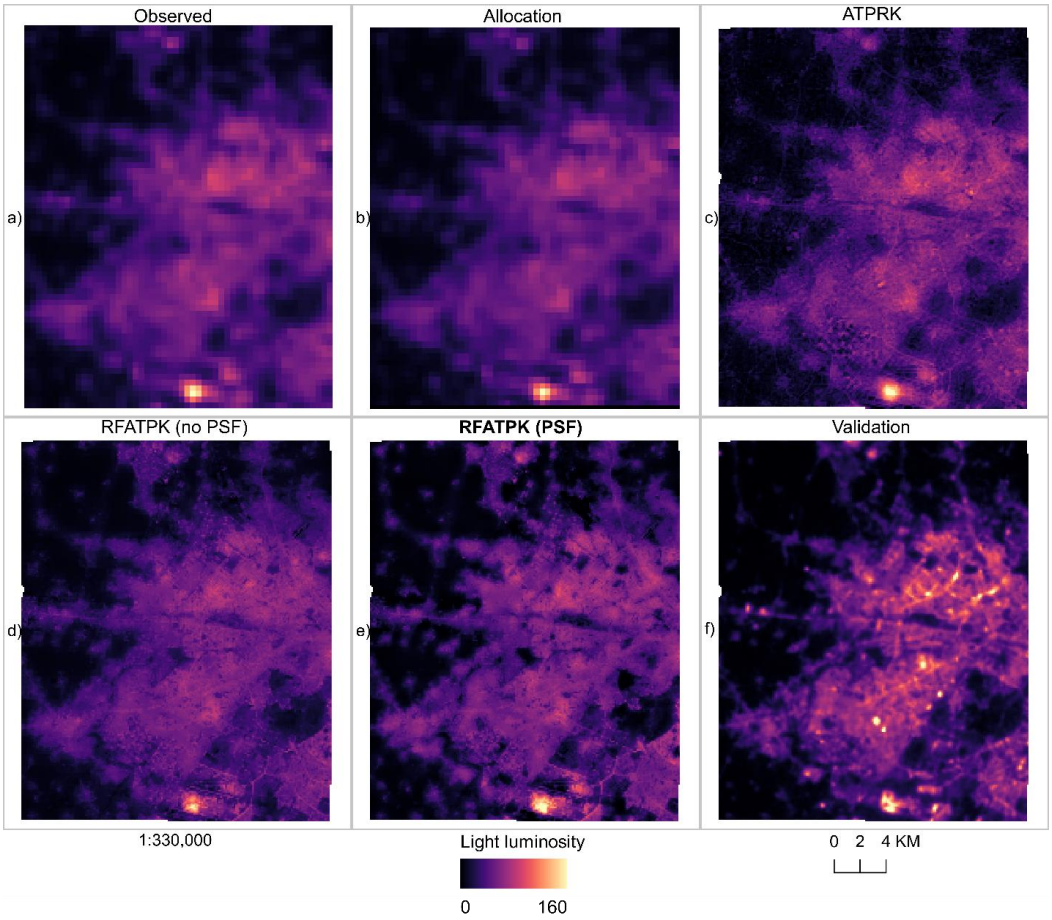

Figure 9. Downscaling results for the various downscaling approaches. a) Observed NTL data, b) Allocation-based downscaling, c) $ATPRK_D$, d) $RFATPK_U$, e) $RFATPK_D$, f) validation NTL data.

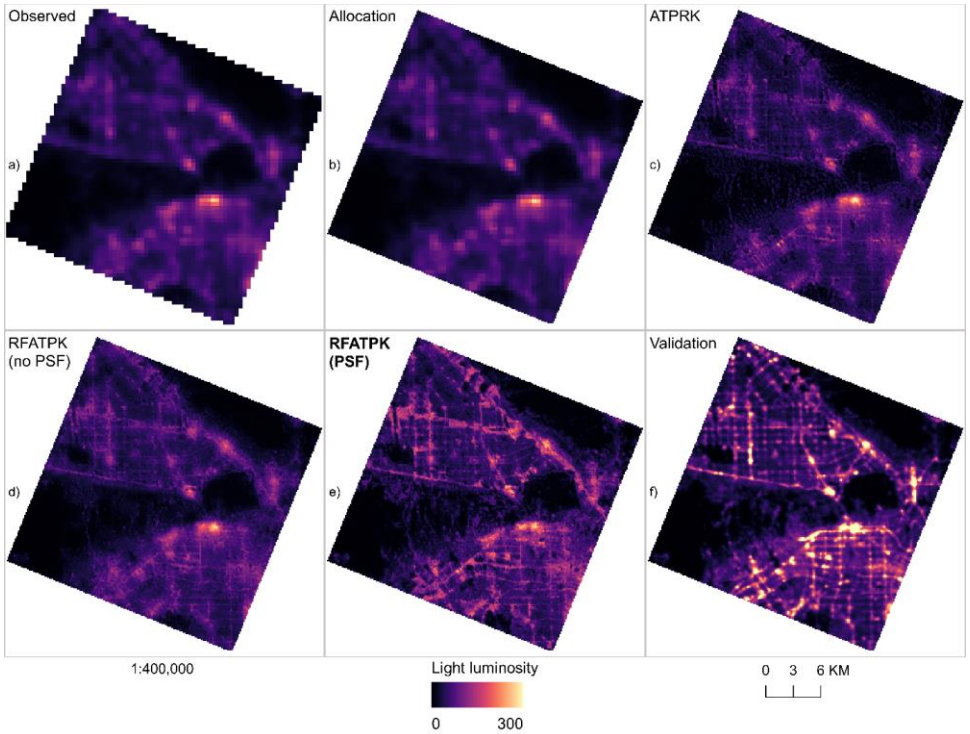

Figure 10. Downscaling results for the various downscaling approaches. a) Observed NTL data, b) Allocation-based downscaling, c) $ATPRK_D$, d) $RFATPK_U$, e) $RFATPK_D$, f) validation NTL data.

Local spatial differences could be noticed for the ATPK-based-downscaling techniques when compared with the validation product, revealed good agreement between the ATPRK and RFATPK downscaling results and Luojia for both megacities. In contrast, the patterns of validation data were not observed via Allocation-based downscaling. Pattern preservation is crucial since the validation data are taken as "true". For both megaregions, although the ATPRK and RFATPK (with and without the PSF) achieved satisfactory visual results, in the disaggregated NTL images using the RFATPK method, the spatial pattern appears clearer. ATPRK downscaled nocturnal imagery shows some outliers in the image for Delhi, indicating areas where the model could not capture well the relationship between the data. $RFATPK_U$, shows spatial details (e.g., road network) clearer compared to the $ATPRK_D$ and $RFATPK_D$.

F. Urban socioeconomic applications

The results of linear regression between the socioeconomic indices and the downscaled NTL data with and without accounting for the PSF are presented in Table 3 below. For both megacities the R^2 between the indices and the downscaled NTL when accounting for the PSF is larger than for the downscaled NTL without accounting for the PSF.

Table IV

R^2 between socioeconomic indices and luminosity (linear regression). In bold are the results with the largest R^2.

Megacity	Index			
	HDI_U	HDI_D	$Income_U$	$Income_D$
Delhi	**0.44**	0.39	**0.24**	**0.24**
LA	**0.21**	**0.21**	**0.71**	0.70

More precisely, for the megacity of Delhi, the R^2 between the HDI and the NTL without the PSF (denoted with subscript D) was 0.39 while for the NTL where the blooming effect was mitigated (denoted with subscript U) was 0.44, a difference of 0.05. For income, the R^2 between the downscaled images was identical for Delhi.

For LA, the association between the HDI_U and NTL was 0.21 and for $Income_U$ was 0.71. On the other hand, the R^2 between the HDI_D and $Income_D$ indices and NTL was 0.21 and 0.70, respectively.

V. DISCUSSION

Very few satellite sensor image enhancing techniques take into account how the neighbors physically influence the central pixel via the PSF effect. While taking the PSF into consideration, the suggested RFATPK method enabled the prediction of NTL at a fine spatial resolution (130 m) with highly satisfactory results. The downscaled data generated have a wide range of potential applications, including those that rely on image processing for remote sensing. The ability to discern the borders more clearly between land cover and land use classes is a significant gain that results from filtering, or minimization of the PSF effect. Two techniques of validation were used to assess the 130 m downscaled predictions: visual and quantitative.

A. Downscaled Results

The 130 m RFTPK predictions for the two experimental regions of Delhi and LA are shown in Figures 5 and 6, respectively. While there are differences overall between the 130 m predictions and the validation data, the bright areas and NTL-free areas have a similar spatial structure. Even while the regression model in the RFATPK technique captured local spatial heterogeneity, it missed certain spatial information, particularly in the NTL extremes, that is the bright areas. This is because RF cannot model extremes well, especially when the distribution is heavily skewed [54]. Predictions in such areas with very high brightness are under-predicted, a phenomenon known as conditional bias [55].

As shown in Figures 5 and 6, the road network for LA and the land cover for Delhi played a crucial role in discriminating NTL luminosity. The results suggest that the method can be generalized to other megacities worldwide where the spatial structure of the road network can be readily obtained either from the fine resolution covariates or the land cover.

B. Fitting model for PSF estimation

The RF model was chosen for estimating the relationship between the coarse and fine bands in Eq. 13. Theoretically, other options like local regression or even spatially weighted regression can be used to quantify the non-linear relationship. When the research area is broad and the data gathering conditions (e.g., viewing angle) vary locally or regionally, these models could be more beneficial since the effective PSF becomes location-dependent [17]. In this instance, an object- or pixel-based estimation of the PSF is possible. However, this spatially adaptive technique could be highly costly to compute, particularly if the research region is very large. In accordance with user needs, the computational burden and PSF estimation accuracy must be suitably balanced.

C. Describing the NTL blooming effect

This research presented a geostatistical solution (RFATPK) that can be used to address the PSF effect on NTL images. There is always a difference in PSF between bands and sensors. To ensure the effectiveness of the geostatistical solutions, the PSF must be characterized precisely. Since the majority of the research currently published claims that the Gaussian filter approximates the true PSF well, we assumed this filter for PSF estimation [16], [18]. However, in practice, the true PSF can be more complicated than the Gaussian filter. The general strategy presented in this paper can be applied to other scenarios with different PSFs, as the implementation of RFATPK is not affected by the particular form of PSF [17].

It would be intriguing to examine various PSFs for both the along-track and across-track orientations [17]. Additionally, hierarchical models may be considered to characterize the PSF. The PSF, for example, may consist of a combination of several filters, such as the triangular and Gaussian filters, or other filters (such as the ideal square wave filter). However, it should be noted that when downscaling, what matters is not the PSF of the original measurements (that is, the path from a point on the ground to a pixel in the image),

but rather the transformation PSF between the original coarse and target fine spatial resolution [17]. This implies that PSF characterization and estimation depend on the quality of the observed coarse and fine bands as well as the sensor; hence, estimation must be done case-by-case. The extent to which prospective alternatives, including nested models, may improve PSF characterization reliability, and how well they can generalize to handle data from other sensors, is unclear.

A small discrepancy was observed between the optimal R^2 in the regression among the megacities. This difference can be explained by the different atmospheric conditions and the number of images involved in the monthly composite. As mention by Bu et al. (2019), among the contributors to the PSF are atmospheric effects and the atmospheric conditions of the particular month (March for Delhi, February for LA). In this research, the focus was the applicability of the method in general, that is, to mitigate the blooming effect during downscaling, and it should be noted that daily images (i.e., not a composite) should be used, where available, to model the *ideal* PSF of the NTL imagery. As stated in Section 2.2, we did not use the daily NTL product here because of the lack of pixels in the study regions due to cloud cover or other quality parameters. In future, we will utilize the daily NTL product from Black Marble (VNP46A2) to investigate the true measurement PSF of a range of NTL sensors.

D. Computational cost

The PSF effect causes a pixel's signal to be tainted by its surrounding pixels. More neighboring pixels are involved when taking the PSF effect into account while downscaling, than when not accounting for the PSF. This is accomplished for ATPK-based solutions using the semivariogram modeling procedure. As seen by Eqs. 8 and 9, convolution considers additional fine pixels from neighbors within the spatial coverage of the PSF, as opposed to standard ATPK, which considers only the center coarse pixel (i.e., without the PSF). The cost of computing will increase as more pixels are considered. The computing time for the two NTL images is displayed in Table 4.

Table V
Processing time of RFATPK for the NTL images for the two megacities.

Megacity	Method	Time (minutes)
Delhi	$ATPK_U$	6.45
	$ATPK_D$	6.27
Los Angeles	$ATPK_U$	25.45
	$ATPK_D$	24.46

The computation time increases from around 28 seconds for Delhi and 1 minute for LA when the PSF is considered. This shows that, to provide more accurate downscaling forecasts, computing performance is in fact compromised when taking the PSF effect into account; yet the overall processing cost (a few seconds) may be considered acceptable. Because of the high level of parallelization of the R package *atakrig* [56] and the coarser spatial resolution of NTL compared to the satellite sensor images, these findings differ from those of Wang et al. [17]. Here, fewer pixels cover the research area(s) compared to the data utilized by Wang et al. [17] (10 m pixel size).

E. Ambiguities in spatial downscaling

Covariates must resemble the brightness in the study region in some way (such as similar spatial structure) to be useful to aid in downscaling. We purposefully avoided additional types of covariates (such as land use data) in this study where the relation with NTL could not be hypothesized explicitly, even though they may have increased the accuracy of downscaling in some cases. We may consider such data in the future because other authors have claimed to be able to enhance regression prediction accuracy [57].

As mentioned previously, RFATPK tends to underpredict regions with extremely high values. It was observed that downscaled NTL was biased in the highest brightness ranges. The difficulty of the RFATPK-based downscaling technique to replicate extremely high value light intensity is probably due to a lack of training data in these brightness ranges, which prevents the RF regression model from being properly calibrated. Extreme gradient boosting, or a different local model like the spatially weighted random forest, or a subset of machine learning known as deep learning (DL), might all be potential solutions for this specific problem. To the best of our knowledge, Wang et al. [58] is the only example of downscaling NTL imaging using DL. Nevertheless, these methods are often computationally costly and need many training points. Although DL techniques have limitations, they are a viable option for modeling non-linear connections and should be considered in further research.

F. Urban socioeconomic applications

Effective criteria must be established to evaluate the differences in socioeconomic development between megacities and track advancement towards the global sustainable development goals. The potential utilization of fine resolution NTL data, which have not been employed widely in related studies, is enhanced by our findings and methodology. The experiments undertaken here demonstrated that downscaled NTL data represent a suitable proxy for measuring socioeconomic differences within megacities. The downscaled NTL data, which accounted for the PSF, reduced the overglow effect inherent in NTL data and increased the ability to represent socioeconomic variables relative to not accounting for the PSF. This means that NTL imagery at a fine resolution produced through the geostatistical approach for sharpening offers a valuable resource for socioeconomic applications, and an alternative to classical methods of measuring human activities.

VI. CONCLUSION

Due to their accessibility and usefulness as proxies, night-time illumination data are utilized frequently in socioeconomic research. However, their spatial resolution is too coarse for many socioeconomic applications, and they are prone to the blooming effect which reduces even further the variation in brightness across pixels within cities and, thus, ultimately reduces the utility of the NTL data. Methods for downscaling remotely sensed images offer a possible solution to the former problem, but until now, the overglow effect in

NTL data due to the PSF has not been addressed when downscaling NTL data. To improve downscaling in the multivariate case and account for the PSF impact while downscaling NTL, RFATPK, a geostatistical-based method, was applied in this research. The experimental findings showed that taking the PSF into account when downscaling generates more accurate predictions at the fine resolution. This benefit was shown to propagate forward to when evaluating social and economic phenomena at the urban scale using the downscaled NTL images.

APPENDIX

Table VI

Calculated spectral indices for the study areas.

Index	Formula
The Enhanced Built-up and Bareness Index (EBBI)	$(SWIR1 - NIR)/(10 * \sqrt{SWIR1 + Thermal})$
The Built-up Area Extraction Index (BAEI)	$(Red + 0.3)/(Green + SWIR1)$
The Built-up Index (BUI)	$\frac{(SWIR1 - NIR)}{(SWIR1 + NIR)} - \frac{(NIR - Red)}{(NIR + Red)}$
The New Built-up Index (NBI)	$(Red - SWIR1)/NIR$
The Normalized Built-up Area Index (NBAI)	$\frac{(\frac{SWIR2 - SWIR1}{Green})}{(\frac{SWIR2 + SWIR1}{Green})}$
The Band Ratio for Built-up Area (BRBA)	$Red/SWIR1$
The Normalized Difference Built-up Index (NDBI)	$(SWIR1 - NIR)/(SWIR1 + NIR)$
The Modified Built-up Area Index (MBAI)	$\frac{[NIR + (1.57 * Green) + (2.4 * SWIR1)]}{(1 + NIR)}$
The Dry Built-up Index (DBI)	$\frac{(Blue - Thermal)}{(Blue + Thermal)} - \frac{(NIR - Red)}{(NIR + Red)}$
The Green Normalized Difference Vegetation Index (GNDVI)	$(NIR - Green)/(NIR + Green)$
The Normalized Difference Vegetation Index (NDVI)	$(NIR - Red)/(NIR + Red)$
The Enhanced Vegetation Index (EVI)	$2.5 * ((NIR - Red)/(NIR + 6 * Red - 7.5 * Blue + 1))$
Modified Normalized Difference Water Index (MNDWI)	$(Green - SWIR1) / (Green + SWIR1)$

ACKNOWLEDGEMENT

We appreciate the thoughtful remarks provided by the anonymous referees, though any deficiencies in the work are our own responsibility.

REFERENCES AND FOOTNOTES

[1] N. Levin *et al.*, "Remote sensing of night lights: A review and an outlook for the future," *Remote Sens. Environ.*, vol. 237, no. September 2019, 2020.

[2] N. Jean, M. Burke, M. Xie, W. M. Davis, D. B. Lobell, and S. Ermon, "Combining satellite imagery and machine learning to predict poverty," *Science (80-.).*, vol. 353, no. 6301, pp. 790–794, 2016.

[3] D. Stathakis and P. Baltas, "Seasonal population estimates based on night-time lights," *Comput. Environ. Urban Syst.*, vol. 68, no. September 2017, pp. 133–141, 2018.

[4] Y. Ye *et al.*, "A feasible framework to downscale NPP-VIIRS nighttime light imagery using multi-source spatial variables and geographically weighted regression," *Int. J. Appl. Earth Obs. Geoinf.*, vol. 104, no. August, p. 102513, 2021.

[5] Q. Zheng, K. C. Seto, Y. Zhou, S. You, and Q. Weng, "Nighttime light remote sensing for urban applications: Progress, challenges, and prospects," *ISPRS J. Photogramm. Remote Sens.*, vol. 202, no. May, pp. 125–141, 2023.

[6] G. Feng, K. Wang, D. Yin, S. Zou, and L. Wang, "How to account for endmember variability in spectral mixture analysis of night-time light imagery?," *Int. J. Remote Sens.*, vol. 41, no. 8, pp. 3147–3161, 2020.

[7] A. Abascal *et al.*, "Mapping the Invisibles: Global Urban Inequalities through Night Lights," *2023 Jt. Urban Remote Sens. Event, JURSE 2023*, no. LMIC, pp. 1–4, 2023.

[8] C. D. Elvidge *et al.*, "The nightsat mission concept," *Int. J. Remote Sens.*, vol. 28, no. 12, pp. 2645–2670, 2007.

[9] P. M. Atkinson, "Downscaling in remote sensing," *Int. J. Appl. Earth Obs. Geoinf.*, vol. 22, no. 1, pp. 106–114, 2013.

[10] P. C. Kyriakidis, "A geostatistical framework for area-to-point spatial interpolation," *Geogr. Anal.*, vol. 36, no. 3, pp. 259–289, Jul. 2004.

[11] Q. Wang, W. Shi, and P. M. Atkinson, "Area-to-point regression kriging for pan-sharpening," *ISPRS J. Photogramm. Remote Sens.*, vol. 114, pp. 151–165, 2016.

[12] N. Tziokas, C. Zhang, G. C. Drolias, and P. M. Atkinson, "Downscaling satellite night-time lights

imagery to support within-city applications using a spatially non-stationary model," *Int. J. Appl. Earth Obs. Geoinf.*, vol. 122, no. April, p. 103395, 2023.

[13] H. Li, L. Jing, C. Dou, and H. Ding, "A Comprehensive Assessment of the Pansharpening of the Nighttime Light Imagery of the Glimmer Imager of the Sustainable Development Science Satellite 1," *Remote Sens.*, vol. 16, no. 2, 2024.

[14] S. Liu *et al.*, "Spatial Downscaling of NPP-VIIRS Nighttime Light Data Using Multiscale Geographically Weighted Regression and Multi-Source Variables," *Remote Sens.*, vol. 14, no. 24, 2022.

[15] J. Guo, F. Zhang, H. Zhao, B. Pan, and L. Mei, "Reconstructing Three-decade Global Fine-Grained Nighttime Light Observations by a New Super-Resolution Framework," pp. 1–34, 2023.

[16] Q. Zheng, Q. Weng, and K. Wang, "Correcting the Pixel Blooming Effect (PiBE) of DMSP-OLS nighttime light imagery," *Remote Sens. Environ.*, vol. 240, no. December 2019, p. 111707, 2020.

[17] Q. Wang, Y. Tang, and P. M. Atkinson, "The effect of the point spread function on downscaling continua," *ISPRS J. Photogramm. Remote Sens.*, vol. 168, no. August, pp. 251–267, 2020.

[18] X. Cao, Y. Hu, X. Zhu, F. Shi, L. Zhuo, and J. Chen, "A simple self-adjusting model for correcting the blooming effects in DMSP-OLS nighttime light images," *Remote Sens. Environ.*, vol. 224, no. June 2018, pp. 401–411, 2019.

[19] M. W. Naikoo, M. Rihan, M. Ishtiaque, and Shahfahad, "Analyses of land use land cover (LULC) change and built-up expansion in the suburb of a metropolitan city: Spatio-temporal analysis of Delhi NCR using landsat datasets," *J. Urban Manag.*, vol. 9, no. 3, pp. 347–359, 2020.

[20] K. Malik, D. Kumar, D. Perissin, and B. Pradhan, "Estimation of ground subsidence of New Delhi, India using PS-InSAR technique and multi-sensor radar data," *Adv. Sp. Res.*, vol. 69, no. 4, pp. 1863–1882, 2022.

[21] K. R. Gurney *et al.*, "The Hestia fossil fuel CO2 emissions data product for the Los Angeles megacity (Hestia-LA)," *Earth Syst. Sci. Data*, vol. 11, no. 3, pp. 1309–1335, 2019.

[22] G. Hulley, S. Shivers, E. Wetherley, and R. Cudd, "New ECOSTRESS and MODIS land surface temperature data reveal fine-scale heat vulnerability in cities: A case study for Los Angeles County, California," *Remote Sens.*, vol. 11, no. 18, pp. 6–8, 2019.

[23] H. Rubinton and M. Isaacson, *Income Segregation and Income Inequality*, vol. 2023, no. 5. 2023.

[24] M. Yuan, X. Li, D. Li, and J. Wu, "An Analysis of Environmental Effect on VIIRS Nighttime Light Monthly Composite Data at Multiple Scales in China," *IEEE J. Sel. Top. Appl. Earth Obs. Remote Sens.*, vol. 16, pp. 825–840, 2022.

[25] Z. Wang, R. M. Shrestha, M. O. Roman, and V. L. Kalb, "NASA's Black Marble Multiangle Nighttime Lights Temporal Composites," *IEEE Geosci. Remote Sens. Lett.*, vol. 19, pp. 1–5, 2022.

[26] M. P. Heris, N. L. Foks, K. J. Bagstad, A. Troy, and Z. H. Ancona, "A rasterized building footprint dataset for the United States," *Sci. Data*, vol. 7, no. 1, pp. 1–10, 2020.

[27] N. Gorelick, M. Hancher, M. Dixon, S. Ilyushchenko, D. Thau, and R. Moore, "Google Earth Engine: Planetary-scale geospatial analysis for everyone," *Remote Sens. Environ.*, vol. 202, pp. 18–27, 2017.

[28] "Geofabrik Download Server." [Online]. Available: https://download.geofabrik.de/. [Accessed: 10-Jun-2023].

[29] M. Schiavina, S. M. Carneiro Freire, and K. MacManus, *GHS population grid multitemporal (1975-2030)*, vol. JRC117104. 2019.

[30] "Global Human Settlement - Datasets - European Commission." [Online]. Available: https://ghsl.jrc.ec.europa.eu/datasets.php. [Accessed: 10-Jun-2023].

[31] "ORNL LandScan Viewer - Oak Ridge National Laboratory." [Online]. Available: https://landscan.ornl.gov/. [Accessed: 10-Jun-2023].

[32] M. F. Archila Bustos, O. Hall, T. Niedomysl, and U. Ernstson, "A pixel level evaluation of five multitemporal global gridded population datasets: a case study in Sweden, 1990–2015," *Popul. Environ.*, vol. 42, no. 2, pp. 255–277, 2020.

[33] H. Ran, F. Zhang, N. W. Chan, M. L. Tan, H. Te Kung, and J. Shi, "New Composite Nighttime Light Index (NCNTL): A New Index for Urbanization Evaluation Research," *IEEE J. Sel. Top. Appl. Earth Obs. Remote Sens.*, vol. 16, pp. 3418–3434, 2023.

[34] "LJ01." [Online]. Available: http://59.175.109.173:8888/app/login_en.html. [Accessed: 10-Jun-2023].

[35] "GADM." [Online]. Available: https://gadm.org/data.html. [Accessed: 10-Jun-2023].

[36] "Esri Land Cover." [Online]. Available: https://livingatlas.arcgis.com/landcover/. [Accessed: 10-Jun-2023].

[37] J. Wu, Z. Zhang, X. Yang, and X. Li, "Analyzing pixel-level relationships between luojia 1-01 nighttime light and urban surface features by separating the pixel blooming effect," *Remote Sens.*, vol. 13, no. 23, pp. 1–21, 2021.

[38] X. Liu and X. Li, "Luojia nighttime light data with a 130m spatial resolution providing a better measurement of gridded anthropogenic heat flux than VIIRS," *Sustain. Cities Soc.*, vol. 94, no. January, p. 104565, 2023.

[39] R. Genuer, J. M. Poggi, and C. Tuleau-Malot, "VSURF: An R package for variable selection using random forests," *R J.*, vol. 7, no. 2, pp. 19–33, 2015.

[40] Q. Wang, W. Shi, P. M. Atkinson, and E. Pardo-Igúzquiza, "A new geostatistical solution to remote sensing image downscaling," *IEEE Trans. Geosci. Remote Sens.*, vol. 54, no. 1, pp. 386–396, 2016.

[41] Q. Wang, Y. Tang, and P. M. Atkinson, "The effect of the point spread function on downscaling continua,"

ISPRS J. Photogramm. Remote Sens., vol. 168, no. April, pp. 251–267, 2020.

[42] P. Goovaerts, "Kriging and semivariogram deconvolution in the presence of irregular geographical units," *Math. Geosci.*, vol. 40, no. 1, pp. 101–128, 2008.

[43] E. Pardo-Iguzquiza, V. F. Rodríguez-Galiano, M. Chica-Olmo, and P. M. Atkinson, "Image fusion by spatially adaptive filtering using downscaling cokriging," *ISPRS J. Photogramm. Remote Sens.*, vol. 66, no. 3, pp. 337–346, 2011.

[44] Q. Wang, W. Shi, P. M. Atkinson, and Y. Zhao, "Downscaling MODIS images with area-to-point regression kriging," *Remote Sens. Environ.*, vol. 166, pp. 191–204, 2015.

[45] J. Xu *et al.*, "Downscaling Aster Land Surface Temperature over Urban Areas with Machine Learning-Based Area-To-Point Regression Kriging," *Remote Sens.*, vol. 12, no. 7, p. 1082, Mar. 2020.

[46] C. Hutengs and M. Vohland, "Downscaling land surface temperatures at regional scales with random forest regression," *Remote Sens. Environ.*, vol. 178, pp. 127–141, 2016.

[47] M. N. Wright and A. Ziegler, "ranger : A Fast Implementation of Random Forests for High Dimensional Data in C++ and R," *J. Stat. Softw.*, vol. 77, no. 1, 2017.

[48] F. Hu, Z. Wei, W. Zhang, D. Dorjee, and L. Meng, "A spatial downscaling method for SMAP soil moisture through visible and shortwave-infrared remote sensing data," *J. Hydrol.*, vol. 590, no. March, p. 125360, 2020.

[49] T. M. Oshiro, P. S. Perez, and J. A. Baranauskas, "How Many Trees in a Random Forest?," in *Lecture Notes in Artificial Intelligence (Subseries of Lecture Notes in Computer Science)*, vol. 2718, 2012, pp. 154–168.

[50] "Global Data Lab - Innovative Instruments for Turning Data into Knowledge." [Online]. Available: https://globaldatalab.org/. [Accessed: 10-Jun-2023].

[51] X. S. Pérez-Sindín, T. H. K. Chen, and A. V. Prishchepov, "Are night-time lights a good proxy of economic activity in rural areas in middle and low-income countries? Examining the empirical evidence from Colombia," *Remote Sens. Appl. Soc. Environ.*, vol. 24, no. September, 2021.

[52] Bu, Xu, Zhang, and Zhang, "Night-light Image Restoration Method Based on Night Scattering Model for Luojia 1-01 Satellite," *Sensors*, vol. 19, no. 17, p. 3761, Aug. 2019.

[53] H. Ebrahimy, H. Aghighi, M. Azadbakht, M. Amani, S. Mahdavi, and A. A. Matkan, "Downscaling MODIS Land Surface Temperature Product Using an Adaptive Random Forest Regression Method and Google Earth Engine for a 19-Years Spatiotemporal Trend Analysis over Iran," *IEEE J. Sel. Top. Appl. Earth Obs. Remote Sens.*, vol. 14, no. Ml, pp. 2103–2112, 2021.

[54] G. B. M. Heuvelink and R. Webster, "Spatial statistics and soil mapping: A blossoming partnership under pressure," *Spat. Stat.*, vol. 50, p. 100639, 2022.

[55] B. Takoutsing and G. B. M. Heuvelink, "Comparing the prediction performance, uncertainty quantification and extrapolation potential of regression kriging and random forest while accounting for soil measurement errors," *Geoderma*, vol. 428, no. May, p. 116192, 2022.

[56] M. Hu and Y. Huang, "atakrig: An R package for multivariate area-to-area and area-to-point kriging predictions," *Comput. Geosci.*, vol. 139, no. June 2019, p. 104471, 2020.

[57] Z. Chen *et al.*, "An extended time series (2000-2018) of global NPP-VIIRS-like nighttime light data from a cross-sensor calibration," *Earth Syst. Sci. Data*, vol. 13, no. 3, pp. 889–906, 2021.

[58] L. Wang *et al.*, "Deep Learning-Based Method To Extend the Time Series of Global Annual Viirs-Like Nighttime Light Data," *Int. Arch. Photogramm. Remote Sens. Spat. Inf. Sci. - ISPRS Arch.*, vol. 43, no. B1-2022, pp. 73–78, 2022.

Nikolaos Tziokas obtained his Bachelor's degree in geography and his Master's degree in geography and applied geoinformatics from the University of the Aegean, Mytilene, North Aegean, Greece, in 2017 and 2019, respectively. Currently, he is pursuing his PhD in geography from the University of Lancaster, Lancashire, UK.

His research interests include remote sensing applications in the urban environment, satellite time-series analysis, geostatistics and geovisualization techniques.

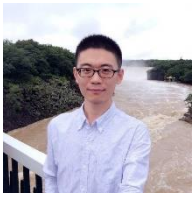

Ce Zhang received Ph.D. Degree in Geography from Lancaster Environment Centre, Lancaster University, U.K. in 2018. He was the recipient of a prestigious European Union (EU) Erasmus Mundus Scholarship for a European Joint MSc programme between the University of Twente (The Netherlands) and the University of Southampton (U.K.). Dr. Zhang is currently a Lecturer in Environmental Data Science at the University of Bristol and a Fellow of UK Centre for Ecology & Hydrology. His major research interests include geospatial artificial intelligence, machine learning, deep learning, and remotely sensed image analysis.

Alexandros Tziokas after attending the Czech Technical University to study computer science, he became an expert in the sector of big data analytics, focusing in backend support and development for big data and business intelligence solutions for companies like DHL, Barclays and NN Group.

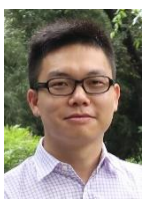

Qunming Wang received the Ph.D. degree from The Hong Kong Polytechnic University, Hong Kong, in 2015.

He was a Lecturer (an Assistant Professor) with the Lancaster Environment Centre,

Lancaster University, Lancaster, U.K., from 2017 to 2018, where he is currently a Visiting Professor. He is currently a Professor with the College of Surveying and Geo-Informatics, Tongji University, Shanghai, China. He has authored or coauthored 90 peer-reviewed articles in international journals such as Remote Sensing of Environment, IEEE Transactions on Geoscience and Remote Sensing, and ISPRS Journal of Photogrammetry and Remote Sensing. His research interests include remote sensing, image processing, and geostatistics.

Prof. Wang is an Editorial Board Member of Remote Sensing of Environment, and serves as an Associate Editor for Science of Remote Sensing (sister journal of Remote Sensing of Environment) and Photogrammetric Engineering & Remote Sensing. He was an Associate Editor of Computers and Geosciences from 2017 to 2020. His three-year Ph.D. study was supported by the hypercompetitive Hong Kong Ph.D. Fellowship and his Ph.D. thesis was awarded as the Outstanding Thesis in the Faculty.

Peter M. Atkinson received the MBA degree from the University of Southampton, Southampton, U.K. in 2012 and the Ph.D. degree (NERC CASE Award with Rothamsted Experimental Station) from the University of Sheffield, Sheffield, U.K. in 1990.

He is currently the Executive Dean of the Faculty of Science and Technology with Lancaster University, U.K. He was previously a Professor of Geography with the University Southampton, where he is currently a Visiting Professor. He is also a Visiting Professor at Tongji University, Shanghai, China. He previously held the Belle van Zuylen Chair with Utrecht University, Utrecht, The Netherlands.

Prof. Atkinson's research interests include remote sensing, geographical information science and spatial (and space-time) statistics applied to a range of environmental science and socio-economic problems. He has run multiple large grants on these themes, and has authored more than 400 peer-reviewed articles in international scientific journals and over 50 refereed book chapters. He has also edited multiple journal special issues and eight books.

Prof. Atkinson is an ISI highly cited researcher and a Fellow of the Learned Society of Wales. He was the 2020 Distinguished Lecturer of the International Association of Mathematical Geosciences and is a recipient of the Peter Burrough Award of the International Spatial Accuracy Research Association. His service contributions include as Editor-in-Chief of *Science of Remote Sensing* and Associate Editor of *Environmetrics*.